Hybrid Extended State Observer-Based Model-Free Predictive Control for Interleaved Buck Converter

Yang Liu, *Senior Member, IEEE*, Xiaoya Mi, Peng Zhang, Yongheng Yang, *Senior Member, IEEE*, Chunyang Zheng, and Yuxuan Pei

***Abstract*—Model predictive control has gained increasing popularity in power electronics in recent years for its simple principle and excellent control performance. However, the traditional model prediction is highly dependent on the mathematical model of the exact system, and the mismatch of system parameters may degrade. Moreover, accurate system modeling remains inherently challenging due to the coexistence of inherent uncertainties and time-varying parametric characteristics. In this regard, a model-free predictive control strategy based on hybrid extended state observer is proposed in this article. It constructs an ultralocal model of the system instead of an accurate physical model to reduce dependence on model parameters. The unmodeled portion of the system is compensated into the unknown terms of the ultralocal model to eliminate steady-state errors and improve the system robustness against disturbances. And the effect of error accumulation in case of model parameter mismatch is reduced. Besides, its stability is analyzed in detail. Finally, a three-phase interleaved buck converter is constructed for simulation and experimental verification. The results show the efficacy of the proposed method with strong robustness.**

***Index Terms*—Hybrid extended state observer (HESO), interleaved buck converter, model-free predictive control (MFPC), robustness, ultralocal model.**

I. Introduction

INTERLEAVING technology is widely used in power electronics converters due to its advantages in reducing current ripple, switching stress and fault tolerance, such as energy storage systems, dc microgrids, photovoltaic power generation, and aerospace [1]. At the same time, complex operating conditions bring more challenges to the system to maintain precise control. Therefore, many advanced control methods, such as sliding mode control [2], fuzzy control [3], and intelligent control [4] have been developed to improve the control performance of the system.

Among them, model predictive control (MPC) has attracted extensive attention owing to its excellent dynamic performance, the possibility of multiobjective optimization and easy implementation [5], [6]. Due to the limitation of computational resources, MPC was initially mainly applied to the control of industrial processes with slow transients. The rapid development of high-performance processors is driving the use of complex control schemes, making MPC more popular in high performance power electronics [7].

Despite significant advantages over conventional control, MPC performance is highly dependent on the model accuracy of the plant. Model mismatches and prediction biases in practice lead to degraded control performance and trajectory deviations. Existing solutions, such as PI-MPC [8] or the addition of an integral term [9] address the steady-state error but can degrade dynamic response by increasing phase lag. In this regard, adaptive model predictive control (AMPC) has been discussed seen from the perspectives of model approximation, parameter identification, and disturbance observation.

For the model approximation method, the system utilizes a series of submodels to simulate dynamic behavior under different operating conditions, which mitigates the impact of parameter uncertainty on the control performance to a certain extent. In [10], a set of linear time-invariant (LTI) models under different operating points was used to describe the converter dynamics and adjust the predictive model accordingly. In [11], the authors have shown that a model logic system based on input–output data can quickly and smoothly identify the system state without any prior knowledge. However, the above two methods need to limit the range of parameter variations, and the prediction accuracy is affected by the size of the model ensemble. Furthermore, adaptive strategies were adopted to update the sensitive parameters of the system in [12] and [13], by designing the adaptive rate of model parameters based on the gradient descent method, where the stability of the closed-loop system was verified. In addition, parameter online identification methods have also been used to identify the unknown parameters in the prediction model. Certain methods include recursive least squares (RLS) [14], [15], observer method [16], fuzzy inference [17], and intelligent algorithm [18]. As for the parameter identification, the problem of identifying parameters that cannot be converged due to under-ranking may occur when the number of parameters to be recognized is too large. A prevalent approach involves predefining subsets of system parameters to decrease the number of parameters requiring identification [19], [20]. However, this will result in biased recognition results when the preset parameters are inaccurate. Another method is to inject an external excitation signal to realize the full rank of

Received 3 April 2025; revised 29 June 2025; accepted 7 August 2025. Date of publication 25 August 2025; date of current version 13 November 2025. This work was supported in part by the National Natural Science Foundation of China under Grant 62473165 and in part by the SSL Sci-tech Commissioner Program under Grant 20234393-01KCJ-G. Recommended for publication by Associate Editor Wilmar Martinez. *(Corresponding author: Peng Zhang.)*

The authors are with the School of Artificial Intelligence and Automation, Huazhong University of Science and Technology (HUST), Wuhan 430074, China (e-mail: pengzh@hust.edu.cn).

Color versions of one or more figures in this article are available at https://doi.org/10.1109/TPEL.2025.3601171.

Digital Object Identifier 10.1109/TPEL.2025.3601171

the model [21], [22], but this method will increase the output harmonics and requires a separate filter design. It should be noted that the aforementioned methods can only suppress the effect of parameter mismatch on the system, but fail to compensate for the disturbance arising from the unmodeled part of the system. This critical limitation has prompted scholarly investigations into a disturbance observer (DOB) that enables estimates such unmodeled perturbations. For instance, in [23], the problem of predictive accuracy enhancement for continuous time MPC is solved by using a perturbation observer, unbiased tracking performance obtained with less computational burdens. In [24], a sliding mode perturbation observer was applied to a current predictive control, method improving the prediction performance.

In addition to the above methods, model-free predictive control (MFPC), an important branch of the MPC field, is gaining increasing attention, with the idea to use sampled data models. The objective of the MFPC is to achieve system prediction and optimal control action calculation with minimal reliance on mathematical models [25]. Current MFPC methodologies can be categorized into three principal approaches based on their model independence levels: 1) Ideal model output error compensation, 2) totally model-free strategies, and 3) hyperlocal modeling techniques in [26]. The first category minimizes discrepancies between ideal and actual system responses. For example, Lee et al. [27] integrated partial feedforward compensation to enhance disturbance rejection under model mismatch, leveraging historical current tracking discrepancies from prior sampling intervals. Advanced implementations strengthen robustness with the aid of adaptive mechanisms by integrating historical switching-state data-driven prediction error correction in feedback-oriented MFPC [28] and online parameter-compensated incremental modeling in adaptive-parameter MFPC [29]. The second methodology eliminates explicit predictive models by executing forecasts through empirical input–output datasets archived in lookup tables, thus bypassing conventional model-based prediction frameworks. Lin et al.[30] proposed an MFPC method only based on a current gradient lookup table, which is simple and easy to implement, but it may suffer from the problem of stagnant lookup table updates. In [31], an improved MFPC was thus developed, which updates the current gradient based on two consecutive measurements.

Another idea is to construct a virtual equivalent model to make MPC model-free, and the most commonly used one is the ultralocal model [32], which uses the unknown terms in the equations to represent certain state variables and the set total perturbations. For example, Zhou et al. [33] employed ultralocal modeling with algebraic parameter identification, theoretically robust yet computationally intensive for real-time systems. To overcome this constraint, Zhang et al. [34] introduced a linear extended state observer (LESO)-based MFPC method, replacing iterative identification with direct state observation to reduce computational burdens. However, the mismatches of control gain cause proportional estimation errors, degrading feedforward compensation and allowing residual disturbances to degrade closed-loop performance.

To address the above issues, this article first analyzes the framework and gain design of the conventional PI controller, with the parameters tuned based on frequency-domain criteria derived from the system's small-signal model. This serves as a baseline for performance comparison. Subsequently, a MFPC structure is developed based on the traditional LESO. The effects of model parameter mismatch on the stability of the observer and the system according to the linear system theory and the Lyapunov theory are analyzed. Subsequently, an improved MFPC control scheme based on HESO is proposed to reduce the effect of parameter mismatch, and to improve the dynamic performance while guaranteeing the system robustness. Finally, the scheme is validated on a three-phase buck converter.

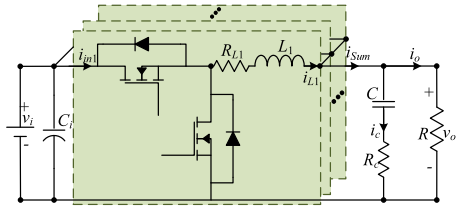

Fig. 1. Topology of interleaved buck converter.

The rest of this article is organized as follows. Section II presents the converter modeling and the basics of the HESO. Section III describes the proposed control method and presents the corresponding analysis. Sections IV shows the simulation and experimental results. Finally, Section V concludes this article.

II. Model of Interleaved Buck Converter

A multiphase interleaved buck converter is shown in Fig. 1, where S_1 and S_2 are power switches of a phase, L_1 and R_{L1} denote its inductor and parasitic resistance, respectively, C_i denotes the input capacitor, C and R_c represent the output capacitor and its parasitic resistance, R represents the equivalent load resistance, v_i and v_o denote the input voltage and output voltage, respectively, i_{Ln} is the nth-phase inductor current, and i_{Sum} and i_o denote total current and the load current, respectively. Its dynamic mathematical model can be expressed as

$$\begin{cases} L_n \frac{\mathrm{d}i_{Ln}(t)}{\mathrm{d}t} = d_n(t)v_i(t) - R_{Ln}i_{Ln}(t) - v_o(t) \\ C\frac{\mathrm{d}v_c(t)}{\mathrm{d}t} = \sum_{n=1}^{N} i_{Ln}(t) - \frac{v_o(t)}{R} \\ CR_c\frac{\mathrm{d}v_c(t)}{\mathrm{d}t} = v_o(t) - v_c(t) \end{cases} \tag{1}$$

where n is the phase index $(n = 1, 2, 3 \cdots N)$.

The ultralocal model of a single-input single-output (SISO) system [32] can be represented as

$$y^{(v)}(t) = bu(t) + F(t) \tag{2}$$

in which y and u represent the input and output variables of the system, respectively, F represents the lumped disturbances of the ultralocal model, and b denotes the control gain of the system. v specifies the order of the plant.

From (1), the n-term interleaved buck converter is an $(n+1)$-order system, where are model parameters are not to easily access. It can be reconfigured as a first-order ultralocal model

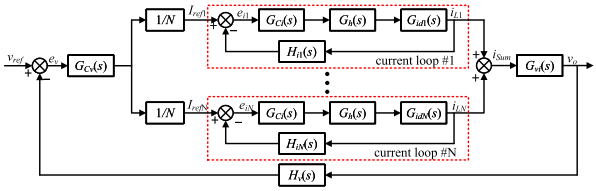

Fig. 2. Block diagram of voltage and current dual-closed-loop PI control.

of the series structure to reduce the system order

$$\begin{cases} \frac{\mathrm{d}i_{Ln}(t)}{\mathrm{d}t} = \frac{v_i(t)}{L_n} d_n(t) - \frac{R_{Ln} i_{Ln}(t) + v_o(t)}{L_n} \\ \frac{\mathrm{d}v_c(t)}{\mathrm{d}t} = \frac{R}{C(R_c+R)} \sum_{n=1}^{N} i_{Ln}(t) - \frac{v_c(t)}{C(R_c+R)}. \end{cases} \tag{3}$$

The capacitor voltages v_c is difficult to obtain. It can be replaced with output voltages v_o approximately.

III. Proposed MFPC Scheme

A. Background

This article takes the widely acknowledged proportional-integral (PI) controller as the fundamental reference framework. The schematic diagram of the PI control structure employed for comparative analysis is illustrated in Fig. 2. The PI controller adopts a dual-loop structure comprising a voltage outer loop and a current inner loop.

The PI gains are determined using frequency-domain stability criteria based on a small-signal model derived from state-space averaging method. For the current loop, the crossover frequency of 16 kHz and the corner frequency of 1.6 kHz are selected in accordance with switching frequency constraints. The proportional K_{ip} and integral gains K_{ii} are calculated by enforcing the magnitude condition $|G_{i0}(j\omega)| = 1$ at $\omega = 2\pi \times 16$ kHz to ensure critical stability, and the pole-zero relationship $K_{\mathrm{ii}}/K_{\mathrm{ip}} = 2\pi \times 1.6$ kHz to optimize transient response. For the voltage loop, similar principles apply, with a lower bandwidth of 200 Hz chosen to ensure loop decoupling. The gains K_{vp} and K_{vi} are obtained by solving analogous frequency-domain equations, yielding a phase margin of 90° and a gain margin of 33.7 dB.

B. Current Loop Design

Based on the ultralocal model, a cascaded control scheme for interleaved buck converters is proposed. The outer loop stabilizes the output voltage and generates the inner loop current reference based on the HESO model-free predictive controller, and the inner loop generates the optimal duty cycle to make the current follow the reference according to the beat-free predictive control principle.

1) LESO Design for Inductor Currents: From the current equation in (3), the mathematical expression for the first-order ultralocal model of the n-phase converter can be given as

$$\begin{cases} \frac{\mathrm{d}i_{Ln}(t)}{\mathrm{d}t} = \frac{v_i(t)}{L_n} d_n(t) + f_{ni}(t) \\ \frac{\mathrm{d}f_{ni}(t)}{\mathrm{d}t} = h(t) \end{cases} \tag{4}$$

where $\frac{v_i(t)}{L_n}$ denotes the control gain b_n of the system. According to (4), the LESO with i_{Ln} and f_{ni} as state variables can be constructed as

$$\begin{cases} e_{ni} = i_{Ln}(t) - z_{n1}(t) \\ \dot{z}_{n1}(t) = b_{0n} d_n(t) + z_{n2}(t) + k_1 e_{ni} \\ \dot{z}_{n2}(t) = k_2 e_{ni} \end{cases} \tag{5}$$

in which z_{n1} and z_{n2} denote the estimates of i_{Ln} and f_{ni}, respectively, and b_{0n} tabulates the controller gain of the converter. The Laplace transform of (5) can be derived as

$$\begin{cases} s z_{n1}(s) = b_{0n} d_n(s) + z_{n2}(s) + k_1 \left[i_{Ln}(s) - z_{n1}(s) \right] \\ s z_{n2}(t) = k_2 \left[i_{Ln}(s) - z_{n1}(s) \right]. \end{cases} \tag{6}$$

Rearranging (6), gives

$$\begin{cases} z_{n1}(s) = \frac{k_1 s + k_2}{s^2 + k_1 s + k_2} I_{Ln}(s) + \frac{b_{0n} s}{s^2 + k_1 s + k_2} D_n(s) \\ z_{n2}(s) = \frac{k_2 s}{s^2 + k_1 s + k_2} I_{Ln}(s) - \frac{b_{0n} k_2}{s^2 + k_1 s + k_2} D_n(s). \end{cases} \tag{7}$$

From the above, the characteristic equation of the second order LESO can be obtained as

$$P(s) = s^2 + k_1 s + k_2. \tag{8}$$

Subsequently, considering the observer gain according to the bandwidth method so that all the roots of the characteristic equation stay in $-\omega_{0i}$, we have $k_1 = 2\omega_{0i}$ and $k_2 = \omega_{0i}^2$. The inductor current observer bandwidth is set to 20 kHz.

Assuming that the sampling frequency of the system is T_s, discretization of (5) using the forward Euler method yields the predicted values of the inductor currents and perturbation estimates as

$$\begin{cases} e_{ni}(k) = i_{Ln}(k) - z_n 1(k) \\ z_{n1}(k+1) = z_{n1}(k) + T_s \left[b_{0n} d_n(k) + z_{n2}(k) + k_1 e_{ni}(k) \right] \\ z_{n2}(k+1) = z_{n2}(k) + k_2 T_s e_{ni}(k). \end{cases} \tag{9}$$

2) MFPC Design for Inductor Currents: In order to ensure that the inner loop has good trajectory tracking characteristics, the cost function with the objective of minimizing inductor current tracking errors can be expressed as

$$J = \left[i_{Lnr} - i_{Ln}(k+1) \right]^2. \tag{10}$$

Substitute (5) into (10) for solution, and considering constraints and the sampling delay of one cycle in the digital system, the inductor current control law can be obtained as

$$d_n(k) = \begin{cases} \frac{i_{Lnr} - z_{n1}(k+1) - z_{n2}(k+1) T_s}{b_{0n} T_s} \\ D_{n,\min}, \quad d_n(k) \le D_{n,\min} \\ D_{n,\max}, \quad d_n(k) \ge D_{n,\max}. \end{cases} \tag{11}$$

The controller gain b_{0n} is analytically determined through the synergistic integration of the hyperlocal model discretization (2) and the control law formulation (11), yielding

$$i_{Ln}(k+1) - i_{Ln}(k) = \frac{b_n}{b_{0n}} \left[i_{Lnr} - z_{n1}(k) - z_{n2}(k) T_s \right] + F(k) T_s. \tag{12}$$

Assuming the system perturbation to be constant, let the error between the current reference and feedback be $e_{rn} = i_{Lnr} - z_{n1}$. The error recursive equation can be obtained as

$$\begin{aligned} e_{rn}(k+1) - e_{rn}(k) = & \left(1-\frac{b_n}{b_{0n}}\right)[e_{rn}(k) - e_{rn}(k-1)] \\ & + \frac{b_n}{b_{0n}} T_s^2 e_{ni}(k-1). \end{aligned} \tag{13}$$

From the above, it can be seen that the convergence of the error is related to the controller gain and the observer error. The observation error is zero under the ideal condition, and thus the gain of the controller should meet: $b_n \le b_{0n}$.

C. Voltage Loop Design

1) HESO Design for Voltage: Let the total inductor currents in the voltage equation be $u_v(t) = \sum_{n=1}^{N} i_{Ln}(t)$. Then, its first-order hyperlocal model can be expressed as

$$\begin{cases} \frac{\mathrm{d}v_o(t)}{\mathrm{d}t} = \frac{R}{C(R_c+R)} u_v(t) + f_v(t) \\ \frac{\mathrm{d}f_v(t)}{\mathrm{d}t} = g(t). \end{cases} \tag{14}$$

Similarly, the LESO with v_o and f_v as state variables can be obtained as

$$\begin{cases} e_v(k) = v_o(k) - z_{v1}(k) \\ z_{v1}(k+1) = z_{v1}(k) + T_s[b_{0v} u_v(k) + z_{v2}(k) + k_{v1} e_v(k)] \\ z_{v2}(k+1) = z_{v2}(k) + k_{v2} T_s e_v(k) \end{cases} \tag{15}$$

where z_{v1} and z_{v2} represent the estimates of v_o and f_v, and b_{0v} is the controller gain. Let the bandwidth of the observer be ω_{0v}, where $\omega_{0v} = 2\pi f_{0v}$. If the bandwidth of the voltage observer f_{0v} is chosen to be 15 KHz, the observer can be obtained as $k_{v1} = 2\omega_{0v}$ and $k_{v2} = \omega_{0v}^2$. When the control gain of the system is not equal to the controller gain, it will cause deterioration in the LESO performance. An improved ESO, which considers adding a correction to the observations to reduce the impact of the control gain deviation is proposed in this article. Discretizing and rearranging (14) gives

$$v_o(k+1) - v_o(k) - f_v(k) T_s = b_v u_v(k) T_s \tag{16a}$$

$$v_o(k) - v_o(k-1) - f_v(k-1) T_s = b_v u_v(k-1) T_s. \tag{16b}$$

Then, it can be obtained that

$$\begin{aligned} f_v(k) = & \frac{v_o(k+1) - v_o(k)}{T_s} - \frac{u_v(k)[v_o(k) - v_o(k-1)]}{u_v(k-1) T_s} \\ & + \frac{u_v(k)}{u_v(k-1)} f_v(k-1). \end{aligned} \tag{17}$$

There are output voltage difference terms in the above equation. In order to reduce the impact of sampling noise, a first-order low-pass filter is applied. Set the bandwidth be ω_{0v} and let $l_0 = T_s\omega_{0v}/(1 + T_s\omega_{0v})$, it can be derived that

$$\hat{f}_{v1}(k) = l_0 f_v(k) + (1 - l_0)\hat{f}_{v1}(k-1) \tag{18}$$

where $\hat{f}_{v1}$ represents the filtered estimates. There is no term associated with b_v in (17) and (18). The effect of controller gain bias on the estimates can be eliminated. However, the method is highly dependent on the previous step estimation results and there is no feedback compensation term. There may be a problem of not converging to the correct value when this method is used alone. Therefore, a new observer that combines the LESO with this method is designed, where β is in the interval of (0,1)

$$\hat{f}_v(k-1) = \beta \hat{f}_{v1}(k-1) + (1-\beta) z_{v2}(k-1) \tag{19a}$$

$$z_{v2}(k) = \beta z_{v2}(k-1) + (1-\beta)\hat{f}_v(k-1) + k_{v2} T_s e_v(k-1). \tag{19b}$$

At last, a low-pass filter is connected between the observer and the controller to increase the rejection of high-frequency noise in the measurement and thus to improve the steady state performance

$$\begin{cases} \theta_1(k+1) = \lambda z_{v1}(k) + (1-\lambda)\theta_1(k) \\ \theta_2(k+1) = \lambda z_{v2}(k) + (1-\lambda)\theta_2(k) \end{cases} \tag{20}$$

in which θ_1 and θ_2 denote the low-pass-filtered value of of z_{v1} and z_{v2}. To keep the performance of the observer, the bandwidth is set to remain at w_{0v}, and $\lambda = w_{0v}T_s/(w_{0v}T_s + 1)$ in the above equation.

2) Controller Design for Output Voltages: To balance the dynamic and steady state performance, both the error of the controlled variable and the deviation of the control quantity will be taken into account when constructing the cost function, which can be expressed as

$$J = [v_{or} - v_o(k+1)]^2 + \rho[u_v(k+1) - u_v(k)]^2. \tag{21}$$

Combining (14)–(21) for solution, and the output voltage control law can be derived as

$$u_v(k) = \begin{cases} \frac{[k_{cv}(v_{or} - \theta_1(k+1)) - \theta_2(k+1)T_s]b_{0v}T_s + \rho u_v(k-1)}{\rho + (b_{0v}T_s)^2} \\ I_{\text{sum,min}}, u_v(k) \le I_{\text{sum,min}} \\ I_{\text{sum,max}}, u_v(k) \ge I_{\text{sum,max}} \end{cases} \tag{22}$$

where I_{sum} is the sum of each branch current of the converter, let the nth branch current distribution coefficient be ϕ_n, then the nth branch current is given as

$$i_{Lnr}(k) = \phi_n u_v(k). \tag{23}$$

When each of the items is completely equalized, $\phi n = 1/N$. Consistent with current-loop controller design principles, the gain of the voltage controller needs to satisfy $b_v \le b_{0v}$. Capacitor parasitic parameters, while inherently small, exhibit significant dependence on temperature, operating frequency, and environmental factors. Moreover, R_c can be ignored, considering that $b_v = 1/C$.

IV. Stability Analysis

A. Observer Performance Analysis

1) Convergence Analysis of LESO: The LESO is in both voltage and current loops, and the LESO in the current loop is taken for analysis. Combining (4) and (5), the error equation for the observer can be derived as

$$\begin{bmatrix} \dot{e}_{n1} \\ \dot{e}_{n2} \end{bmatrix} = \begin{bmatrix} -2\omega_{0i} & 1 \\ -\omega_{0i}^2 & 0 \end{bmatrix} \begin{bmatrix} e_{n1} \\ e_{n2} \end{bmatrix} + \begin{bmatrix} 0 \\ 1 \end{bmatrix} h \tag{24}$$

where $e_{n1} = i_{Ln}(t) - z_{n1}(t)$ and $e_{n2} = f_{ni}(t) - z_{n2}(t)$. e_{n1} and e_{n2} represent the observation errors for the inductor current

and disturbance, respectively, and h denotes the derivative of the perturbation.

Let $\varepsilon_k = e_{nk}/(\omega_{0i})^{k-1}$, then the above equation can be reconstructed as

$$\begin{bmatrix}\dot{\varepsilon}_1\\ \dot{\varepsilon}_2\end{bmatrix} = \omega_{0i}\underbrace{\begin{bmatrix}-2 & 1\\ -1 & 0\end{bmatrix}}_{\boldsymbol{A_\varepsilon}}\underbrace{\begin{bmatrix}\varepsilon_1\\ \varepsilon_2\end{bmatrix}}_{\boldsymbol{\varepsilon}} + \underbrace{\begin{bmatrix}0\\ 1\end{bmatrix}}_{\boldsymbol{B_\varepsilon}}\frac{h}{\omega_{0i}} \tag{25}$$

from which, the solution for the observation error can be expressed as

$$\boldsymbol{\varepsilon}(t) = e^{\boldsymbol{A_\varepsilon} w_{0i} t}\boldsymbol{\varepsilon}(0) + \int_0^t e^{\boldsymbol{A_\varepsilon} w_{0i}(t-\tau)}\boldsymbol{B_\varepsilon}\frac{h}{w_{0i}}\mathrm{d}\tau \tag{26}$$

where $\boldsymbol{\varepsilon}(0) = [\varepsilon_1(0) \quad \varepsilon_2(0)]^T = [e_{n1} \quad \frac{e_{n2}}{\omega_{0i}}]^T$ is the initial observation error.

Assume that the derivative of the lumped disturbance $h(t)$ is bounded, there is constant H, such that $|h(t)| \le H$. Let $\varphi(t) = \int_0^t e^{\boldsymbol{A_\varepsilon} w_{0i}(t-\tau)}\boldsymbol{B_\varepsilon}\frac{h}{w_{0i}}\mathrm{d}\tau$, then

$$\begin{aligned}\|\varphi(t)\| &\le \|\frac{H}{w_{0i}^2}\left(\boldsymbol{A_\varepsilon}^{-1}\boldsymbol{B_\varepsilon} - \boldsymbol{A_\varepsilon}^{-1}e^{\boldsymbol{A_\varepsilon} w_{0i} t}\boldsymbol{B_\varepsilon}\right)\| \\ &\le \frac{H}{w_{0i}^2}\left(\|\boldsymbol{A_\varepsilon}^{-1}\boldsymbol{B_\varepsilon}\| + \|\boldsymbol{A_\varepsilon}^{-1}e^{\boldsymbol{A_\varepsilon} w_{0i} t}\boldsymbol{B_\varepsilon}\|\right).\end{aligned} \tag{27}$$

The inverse of the matrix $\boldsymbol{A_\varepsilon}$. The inverse of matrix $\boldsymbol{A}$ exists and is unique. It can be easily derived

$$\boldsymbol{A_\varepsilon}^{-1}\boldsymbol{B_\varepsilon} = \begin{bmatrix}0 & -1\\ 1 & -2\end{bmatrix}\begin{bmatrix}0\\ 1\end{bmatrix} = \begin{bmatrix}-1\\ -2\end{bmatrix}. \tag{28}$$

The matrix $\boldsymbol{A_\varepsilon}$ is a Hurwitz matrix and its eigenvalues are $\lambda_{1,2} = -1$. Then

$$e^{\boldsymbol{A_\varepsilon} w_{0i} t} = \frac{\boldsymbol{P_\varepsilon}(t)}{e^t} = \frac{\boldsymbol{P_\varepsilon}(t)}{1 + t + \frac{t^2}{2} + \cdots + \frac{t^n}{n!}} \tag{29}$$

where $\boldsymbol{P_\varepsilon}(t)$ represents a first-order polynomial matrix in t. This matrix asymptotically converges to zero, with its convergence rate governed exclusively by the observer bandwidth

$$\begin{aligned}\|\boldsymbol{\varepsilon}(t)\|_{\lim_{t\to\infty}} &= \|e^{\boldsymbol{A_\varepsilon} w_{0i} t}\boldsymbol{\varepsilon}(0)\|_{\lim_{t\to\infty}} + \|\varphi(t)\|_{\lim_{t\to\infty}} \\ &\le \tfrac{H\|\boldsymbol{A_\varepsilon}^{-1}\boldsymbol{B_\varepsilon}\|}{\omega_{0i}^2} = \tfrac{\sqrt{5}H}{\omega_{0i}^2}.\end{aligned} \tag{30}$$

From (30), the observation error is related to the derivative bounds of the lumped disturbance and the bandwidth of the observer. It can track the step disturbance without bias.

When the system control gain b_n is not equal to the controller gain b_{0n}, the ultralocal model is expressed as

$$\dot{i}_{Ln} = b_n d_n + f_{ni} = b_{0n} d_n + \underbrace{(b - b_{0n})\, d_n + f_{ni}}_{f} \tag{31}$$

in which, the new lumped disturbance term contains variables that introduce high-frequency terms to the original disturbances. This will negatively affect the performance the entire system.

2) Convergence Analysis of HESO: To simplify the analysis, assume that the lumped disturbance is a constant F, and set $e_{\hat{f}} = F - \hat{f}_v$, $e_{z2} = F - z_{v2}$. According to (19a) it can be obtained that

$$\begin{aligned}e_{\hat{f}}(k+1) - e_{\hat{f}}(k) &= (1-\beta)[e_{z2}(k) - e_{z2}(k-1)] \\ &+ \beta(1-l_0)[e_{\hat{f}}(k) - e_{\hat{f}}(k-1)] + \beta l_0[f(k-1) - f(k)] \\ &= \Delta e_f + \Delta e_{z2} + \Delta e_{\hat{f}}\end{aligned} \tag{32}$$

where the convergence of $\hat{f}_v$ is determined by three components. f is derived from the control variable u_v and differential of v_o. Provided that the system satisfies the asymptotic stability condition, there must be $\Delta e_f = 0$ when the system reaches its steady state. However, the terminal value of $f(k)$ is not certain, and e_{z2} is exclusively determined by LESO. Based on the preceding convergence analysis of the inductor current observer, it can be derived that $\Delta e_{z2} \le 0$. Meanwhile, $\Delta e_{z2} \le 0$. $\Delta e_{\hat{f}}$ is contingent upon both the initial state and the filtering time constant, with its convergence rate being intrinsically linked to the parameter l_0.

According to the above analysis, the part represented by (19a) is convergent. Since (19b) integrates the LESO together with (19a), it is easy to obtain that the proposed HESO is also convergent.

B. Closed-Loop Performance Analysis

The current loop is first analyzed by assuming that the ratio of the actual system gain b_n to the controller gain b_{0n} is $k_{bn} = \frac{b_n}{b_{0n}}$. Combining (4), (5), and (11), the closed-loop transfer function can be derived as

$$G_{ci}(s) = \frac{i_{Ln}(s)}{i_r(s)} = \frac{\frac{k_{bn}}{T_s}\left(s^2 + k_1 s + k_2\right)}{s^3 + k_1 s^2 + k_2 k_{bn} s + \frac{k_{bn}}{T_s}\left(s^2 + k_1 s + k_2\right)}. \tag{33}$$

In particular, when $k_{bn} \approx 1$, the current loop can be equated to an inertial link as shown in (34), while the bandwidth is independent on the observer

$$\frac{i_{Ln}(s)}{I_r(s)} \approx \frac{k_{bn}}{T_s s + k_{bn}}. \tag{34}$$

Based on (33), the characteristic equation with respect to k_{bn} is reformulated as

$$1 + k_{bn}\frac{\frac{1}{T_s}\left(s^2 + k_1 s + k_2\right) + k_2 s}{s^3 + k_1 s^2} = 0. \tag{35}$$

The root-locus of the current closed-loop as k_{bn} varies from 0 to 2.1386 is shown in Fig. 3. It can be seen that the characteristic root lies outside the unit circle when $k_{bn} = 2.1386$, the system is unstable. Therefore, k_{bn} cannot be too large, which is basically consistent with the previous analysis.

The closed-loop Bode plot of the system when $k_{bn} \le 1$ is shown in Fig. 4. There is a certain degree of decrease in the closed-loop bandwidth of the system when k_{bn} changes from 1 to 0.7. But the current loop still has a high bandwidth with negligible overall performance impact. In order to ensure that the system has a sufficiently large stability margin, $k_{bn} = 0.7$ is selected.

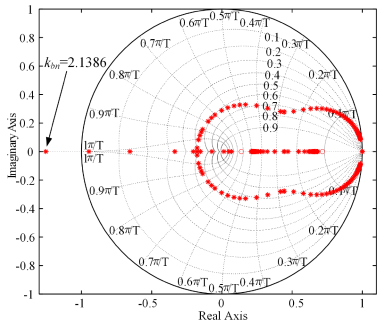

Fig. 3. Root-locus of the current closed-loop with respect to k_{bn}.

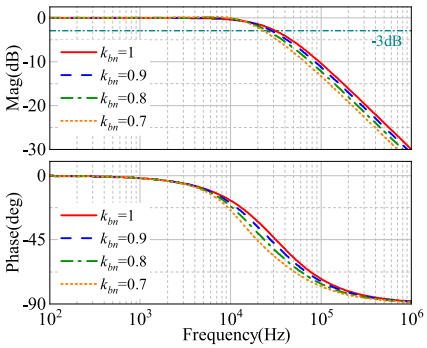

Fig. 4. Closed-loop Bode plot for the current loop.

Let $\frac{u_v(k)}{u_v(k-1)} = \eta_k$, the Z-transformation of (17) can be derived as

$$f_v(z) = \frac{1-z^{-1}\eta_k}{1-z^{-1}\eta_k}\frac{z-1}{T_s}v_o(z) = \frac{z-1}{T_s}v_o(z) \tag{36}$$

from which, f_v can be by replaced with the first-order derivative of the output voltage approximately. Neglect the effect of the filters and take it into (19b), z_{v2} in the S-domain can be expressed as

$$z_{v2}(s) = \frac{k_{v1}T_\beta\left[v_o(s)-z_{v1}(s)\right]}{T_\beta s+1} + \frac{sv_o(s)}{T_\beta s+1} \tag{37}$$

where $T_\beta = T_s/(1-\beta)$. The current loop is replaced with the first-order inertial link depicted in (34). Assuming the filtering time constant of this element to be T_1, it is defined as $T_1 = T_s/k_{bn}$. By setting the external disturbance $f_v = 0$ and simplifying calculations with $\rho = 0$, the governing transfer function can be derived as follows:

$$\begin{cases} sv_o(s) = b_v G_1(s) i_{rn}(s) \\ i_{rn}(s) = \frac{k_{cv}[v_{or}(s)-v_o(s)]-z_{v2}(s)}{b_{0v}T_s} \\ sz_{v1}(s) = b_{0v}u_v(s) + z_{v2}(s) + k_{v1}[v_o(s)-z_{v1}(s)] \\ sz_{v2}(s) = k_{v2}[v_o(s)-z_{v1}(s)]. \end{cases} \tag{38}$$

By solving (38), a simplified system control block diagram can be obtained as shown in Fig. 5. Let $k_{v0} = k_{cv}/T_s$ and $k_{bv} = b_v/b_{0v}$, where k_{cv} denotes the actual control gain, and k_{bv} represents the ratio between the actual control gain and the voltage controller gain. Consequently, the equations are given

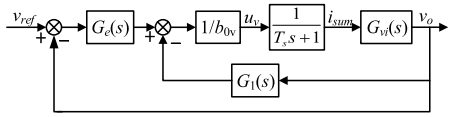

Fig. 5. Simplified diagram of the control system.

by

$$\begin{cases} G_e(s) = k_{bv}k_{v0} + \frac{k_{v2}k_{v0}T_\beta}{(1+T_\beta s)(s+k_{v1})} \\ G_f(s) = \frac{k_{v2}T_\beta+s}{(1+T_\beta s)} - \frac{k_{v1}k_{v2}T_\beta}{(1+T_\beta s)(s+k_{v1})}. \end{cases} \tag{39}$$

Furthermore, the closed loop transfer function of the system can be derived as

$$\frac{v_o(s)}{v_r(s)} = \frac{k_b k_{v0}\left[T_\beta s^2+(T_\beta k_{v1}+1)\,s+(k_{v1}+T_\beta k_{v2})\right]}{a_4 s^4+a_3 s^3+a_2 s^2+a_1 s+a_0} \tag{40}$$

where

$$\begin{aligned} a_4 &= T_\beta T_s,\, a_3 = T_\beta T_s k_{v1} + T_s + T_\beta \\ a_2 &= T_s k_{v1} + T_\beta k_{v1} + 1 + k_{bv} + T_\beta k_{bv} k_{v0} \\ a_1 &= k_{v1} + k_{bv}k_{v0}\left(T_\beta k_{v1}+1\right) + k_{bv}k_{v1} + T_\beta k_{bv}k_{v2} \\ a_0 &= k_{bv}k_{v0}\left(k_{v1}+T_\beta k_{v2}\right). \end{aligned}$$

Similarly, the characteristic equation with respect to T_β derived from (40) can be expressed as

$$\begin{aligned} &T_s s^4+(T_s k_{v1}+1)s^3+ \\ &T_\beta\frac{(k_{v1}+k_{bv}k_{v0})s^2+k_{bv}(k_{v0}k_{v1}+k_{v2})s+k_{bv}k_{v0}k_{v2}}{T_s s^3+(T_s k_{v1}+1+k_{bv})s^2+\left[k_{bv}(k_{v0}+k_{v1})+k_{v1}\right]s+k_{bv}k_{v1}k_{v0}}+1=0 \end{aligned} \tag{41}$$

$$G_{ov1}(s)H(s) = \frac{k_{bv}k_{v0}\left(s^2+k_{v1}s+k_{v2}\right)}{T_1 s^4+(1+k_{v1}T_1)s^3+k_{v1}s^2+k_{v2}k_{bv}s} \tag{42}$$

$$\begin{aligned} \frac{v_o(s)}{v_{or}(s)} = &\frac{k_{bv}k_{v0}\left(s^2+k_{v1}s+k_{v2}\right)}{T_1 s^4+(1+k_{v1}T_1)s^3+(k_{v1}+k_{bv}k_{v0})s^2} \\ &+\frac{(k_{v2}k_{bv}+k_{v1}k_{bv}k_{v0})s+k_{v1}k_{bv}k_{v0}}{T_1 s^4+(1+k_{v1}T_1)s^3+(k_{v1}+k_{bv}k_{v0})s^2}. \end{aligned} \tag{43}$$

The voltage-loop open-loop and closed-loop transfer functions under LESO scheme are respectively given in (42) and (43). Following analogous derivation procedures to the previous, the mathematical proofs are therefore omitted for conciseness. The root-locus of the voltage closed-loop as the parameter T_β varies is shown in Fig. 6. When $T_\beta = 0$, the characteristic root lies on the unit circle, while the system is in critical stability. When $T_\beta > 0$, the closed-loop characteristic root of the system lies in the unit circle, and it is always stable. It has been previously defined that β is in the interval (0,1), so the HESO control strategy does not affect the closed-loop stability of the system. The design simulation parameter $\beta = 0.6$.

The closed-loop bode plot of the voltage loop when $k_{bv} \le 1$ is shown in Fig. 7. It can be seen that the amplitude-frequency

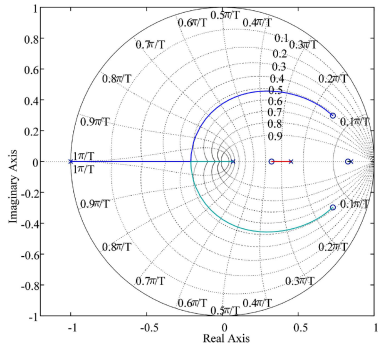

Fig. 6. Root-locus of the voltage closed-loop with respect to T_β.

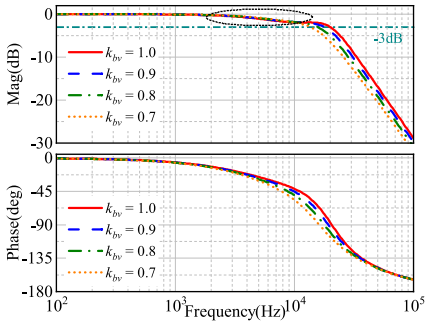

Fig. 7. Closed-loop Bode plot for voltage loop with respect to k_{bv}.

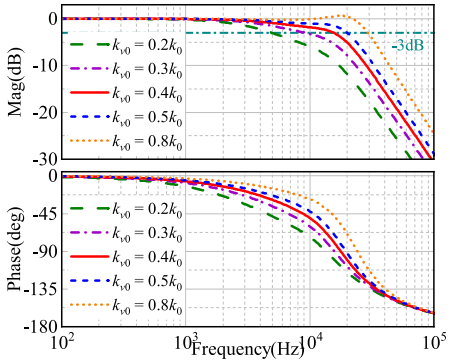

Fig. 8. Closed-loop Bode plot for voltage loop with respect to k_{cv}.

curves overlap within the bandwidth of the voltage loop when k_{bv} varies, which reduces the impact of parameter mismatch. When LESO is employed, the k_{bv} is reduced from 1.0 to 0.7, and the maximum increase in voltage amplitude in the midfrequency band is about 1 dB. In contrast, the amplitude-frequency curves overlap within the bandwidth of the voltage loop when k_{bv} varies with the implementation of HESO, which reduces the impact of parameter mismatch. However, the shortcoming is that it may cause a drop in gain in the middle and high frequency bands. This problem can be solved by increasing the controller gain k_{cv}.

As the controller gain k_{v0} varies, the closed-loop Bode plot of the voltage loop is shown in Fig. 8,where $k_0 = 1/T_s$. It

TABLE I
CIRCUIT PARAMETERS OF INTERLEAVED BUCK CONVERTS

Variables	Quantity	Nominal Values
v_o	Output voltage	15 V
v_i	Input voltage	30 V
f_s	Switching frequency	200 kHz
L_1 ,L_2 ,L_3	Filter inductors	33 μH
C	Output capacitor	150 μF
P_o	Output power	180 W

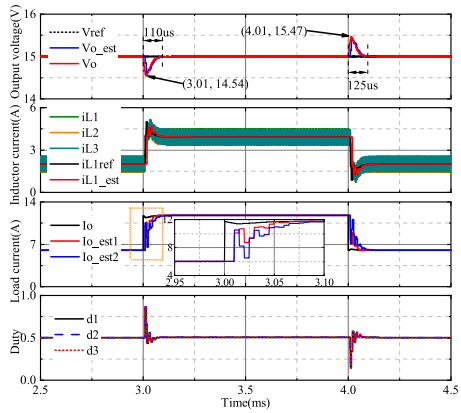

Fig. 9. Simulation results under step load disturbance.

can be seen that the control performance of the system is mainly influenced by k_{v0}. Meantime, increasing k_{v0} can improve the closed-loop bandwidth of the system. LESO implementation exhibits a resonance peak in the amplitude-frequency characteristic at $k_{v0} = 0.4k_0$, accompanied by output voltage overshoot. Conversely, HESO method eliminates resonant phenomena through midfrequency gain attenuation, maintaining flat amplitude-frequency characteristics. When k_{v0} increases to $0.8k_0$, the amplitude-frequency characteristic curve appears resonance peaks, while there is an output voltage overshoot. Considering the control performance of the system, the design is $k_{v0} = 0.3k_0$ when LESO is used and $k_{v0} = 0.4k_0$ when HESO is employed.

V. SIMULATION AND EXPERIMENTAL RESULTS

To verify the above theoretical analysis, a simulation model based on the proposed method is built in Matlab/Simulink, and experimental verification is carried out on a three-phase interleaved buck converter prototype. The circuit parameters of the converter are given in Table I. The sampling rate of the inductor current and output voltage are both 200 kHz. Maximum inductor current reference is 10 A.

Fig. 9 shows the simulation results under step load change. The load current steps from 6 to 12 A at 3 ms. After about three switching cycles, the inductor current keeps up with the load current after three steps, output voltage drops about 0.46 V, and

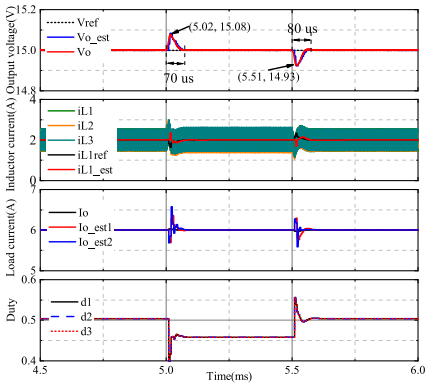

Fig. 10. Simulation results under step v_i disturbance.

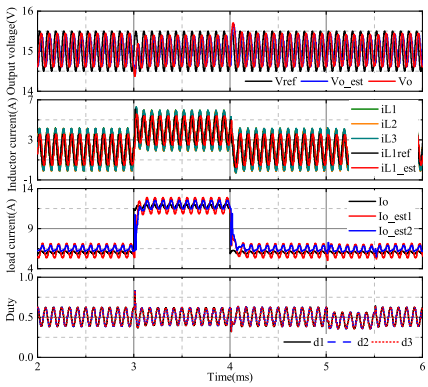

Fig. 11. Simulation results of sinusoidal reference tracking.

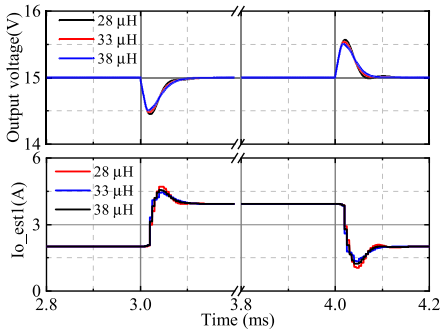

Fig. 12. Influence of filter inductors on system performance under step load disturbance.

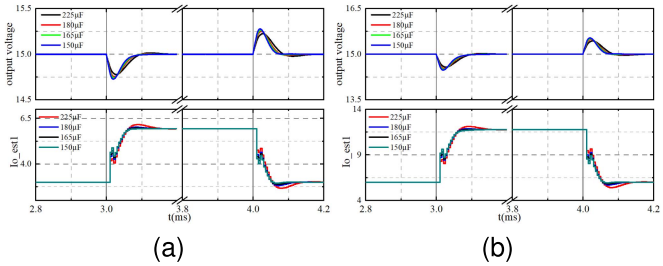

Fig. 13. Influence of output capacitor on system performance under step load disturbance. (a) In 50% full load. (b) In 100% full load.

TABLE II
PERFORMANCE OF HESO-MFPC CONTROLLER AT DIFFERENT LOAD CONDITIONS

Capacitance	Parameter	Load Conditions			
		25%FL	50%FL	75%FL	100%FL
150μF	recovery time (μs)	103	110	119	133
	overshoot (%)	0.93	1.82	2.67	3.47
165μF	recovery time (μs)	118	125	130	136
	overshoot (%)	0.89	1.72	2.53	3.29
180μF	recovery time (μs)	138	141	147	152
	overshoot (%)	0.81	1.65	2.41	3.15
225μF	recovery time (μs)	161	172	184	190
	overshoot (%)	0.76	1.47	2.17	2.85

the dynamic recovery time is 110 μs. The load current steps back to 6 A at 4 ms, the output voltage has an overshoot of 0.47 V, and the dynamic recovery time is about 125 μs. Maximum deviation between estimated and actual output voltage during transients is less than 0.3 V, about 2% of the rated voltage. The inductor current estimate is essentially the same as the average value with good tracking characteristics. Io_{est1} and Io_{est2} are the converted values of the disturbance estimates z_{v2} and $\hat{f}_v$ multiplied by C_0. z_{v2} converges to the true value after 10 steps. $\hat{f}_v$ converges slower than z_{v2}.

A. Simulation Results

Fig. 10 shows the simulation results under a step change of v_i. The input voltage steps from 30 to 33 V at 5 ms, and it goes back to 30 V at 5.5 ms. The output voltage fluctuation is about 0.51%. The dynamic recovery time less than 80 μs. The convergence rates of z_{v2} and $\hat{f}_v$ are essentially the same under the input voltage disturbance.

Fig. 11 shows the simulation results of sinusoidal reference tracking. The reference value of the output voltage is set to $v_r = 15 + 0.5\sin(24 \times 10^3 \pi t)$. The amplitude of the ac component is 0.42 V. The phase lag is about 79°. The observers for the output voltage and inductor current still converge well. As it can be seen from the Fig. 11, z_{v2} has good sinusoidal properties. However, a nonlinear distortion is present in the estimated disturbance $\hat{f}_v$, which introduces a small dc bias in the output voltage. Despite this perturbation, the output voltage waveform maintains excellent sinusoidal fidelity with negligible distortion.

In practical applications, the quality of the components will degrade during operations, and it will affect the control performance of the entire power converter. Assuming that the allowable variation range of inductance is 15% and the allowable variation range of capacitance is 50%, the simulation results obtained under a load step are shown in Figs. 12 and 13. It can be seen that when the inductance parameter is varied, the effect on the output voltage is small. The change in capacitance has a relatively larger effect on the output voltage, but the proposed method still maintains good dynamic performance in Fig. 13. Table II presents a comparative analysis of transient

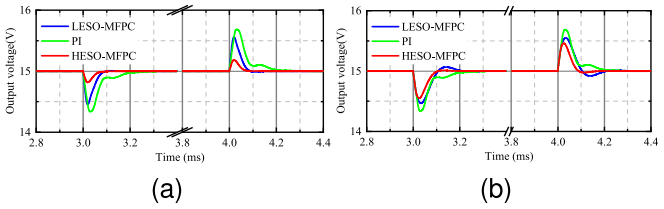

Fig. 14. Simulation results under step load disturbance with three control methods. (a) When the parameters are matched. (b) When the capacitors are mismatched.

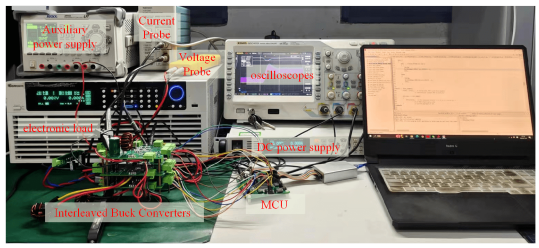

Fig. 15. Experimental platform of the interleaved buck converter.

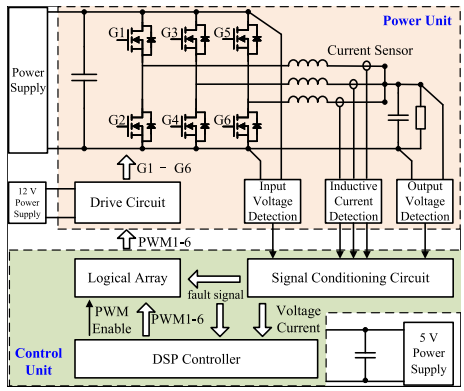

Fig. 16. Block diagram of the overall control structure.

performance metrics, revealing load-dependent capacitance effects on overshoot and recovery dynamics. Elevated capacitance from 150 μF to 225 μF yields 0.62% overshoot reduction but prolongs recovery time, whereas reduced capacitance enhances light-load transient speed at the cost of voltage regulation under heavy loads. For instance, a 150 μF capacitor exhibits 103 μs recovery with 0.93% overshoot at 25% load, worsening to 133 μs and 3.47% overshoot under full load. As can be observed in Fig. 14, the output voltage waveforms generated by three different control schemes under parameter-matched and mismatched conditions are presented. It can be seen that, when parameters are matched, the proposed HESO-MFPC scheme achieves 2.51% and 3.69% peak overshoot attenuation relative to LESO-MFPC and PI, respectively, with corresponding transient recovery duration reductions of 20 and 192 μs. This is consistent with the theoretical analysis in the previous section.

Under parameter mismatch conditions, comparative analysis of control strategies reveals significant performance differences. The conventional dual-closed-loop PI control exhibits a substantial voltage sag of 0.7 V with prolonged transient recovery duration approximately 300 μs. When implementing the MFPC based on LESO, comparative metrics show a 0.9% relative decrease in overshoot magnitude, accompanied by reduced transient recovery time to 200 μs. Notably, the proposed MFPC based on HESO minimizes voltage deviation duration to 161 μs, while maintaining overshoot at 0.5 V. The HESO method shows better performance during load perturbations since the filtered perturbation estimates are independent of the system control gain, reducing the dependence on the model. These results confirm the superiority of the proposed MFPC in dynamic regulation and disturbance rejection capabilities.

B. Experimental Validations

Experimental platform of the interleaved buck converter is presented in Fig. 15. It consists of two dc power supplies, three-phase buck converts and an electronic load. The circuit parameters and sampling rates are the same as that in simulations. The block diagram of the overall control structure is depicted in Fig. 16. It mainly contains the power unit and control unit. The power unit is fundamentally composed of the power circuit, the voltage and current signal detection circuit, as well as the drive circuit. Meanwhile, the control unit comprises the signal conditioning circuit, the logic array, and the DSP controller. The controller adopts a dual-core processor, TMS320F28377D, with its operating frequency being 200 MHz. The memory usage of these three methods is illustrated in Table III. HESO eliminates reliance on state equation iteration in (19a), thereby, circumventing the vector recursive computation in LESO's discretized formulation in (15). Therefore, compared with LESO, there is a slight reduction in memory usage.

TABLE III
MEMORY USAGE COMPARISON

Parameter	PI	LESO-MFPC	HESO-MFPC
RAM (KB)	34.61	34.64	34.63
FLASH (KB)	8.71	8.47	8.43

Experimental results under step load disturbance is shown in Figs. 17 and 19. Rated working condition of the full load current is 12 A, the set load current change rate is 0.5 A/μs. When the load is increased, the output voltage drops by 1.16 V, with the regulation time of about 272 μs. When the load is decreased, the output voltage has an overshoot of 1.08 V, with the regulation time of 272 μs. It is closer to the simulation results, but the steady state fluctuation of the inductor current is larger due to the sampling noise.

In order to test the robustness of the system, the load step test is carried out under the mismatch of inductor and capacitor parameters.

Given the complexity involved in physical inductor replacement, the simulation of actual inductor parameter mismatch is

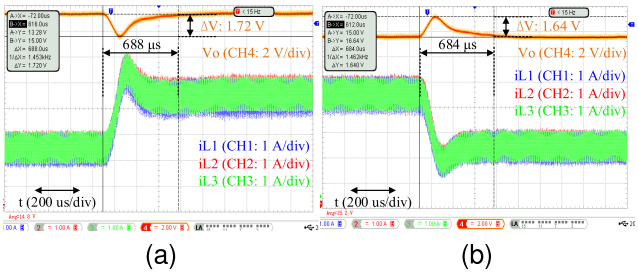

Fig. 17. Experimental results under step load disturbance using PI controller. (a) Load current steps from 6 A to 12 A. (b) Load current steps from 12 to 6 A.

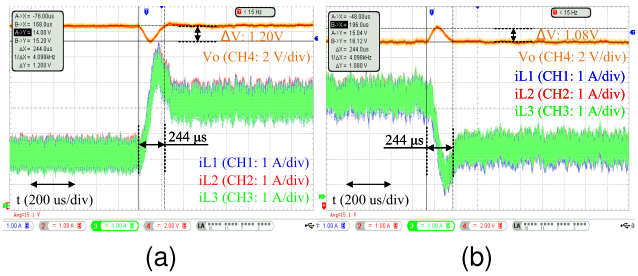

Fig. 18. Experimental results under step load disturbance using LESO-MEPC controller. (a) Load current steps from 6 to 12 A. (b) Load current steps from 12 to 6 A.

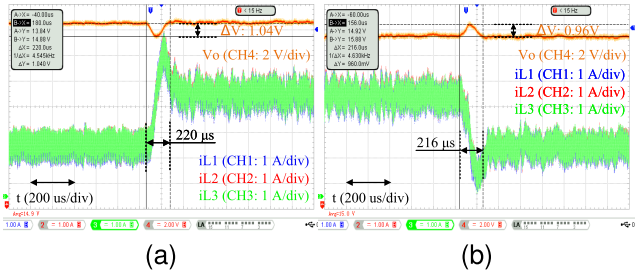

Fig. 19. Experimental results under step load disturbance using HESO-MEPC controller: (a) Load current steps from 6 to 12 A. (b) Load current steps from 12 to 6 A.

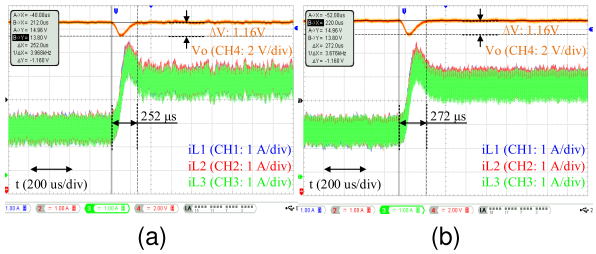

Fig. 20. Experimental test of load disturbance when inductance parameter changes. (a) Inductance parameter is increased to 38 μH. (b) Inductance parameter is reduced to 28 μH.

achieved by modifying the inductor parameters in the controller. With inductor variations constrained within $\pm$ 15% bounds, the inductor parameters are set to be 38 and 28 μ H. The experimental results are shown in Fig. 20. When the inductance parameter of the controller is increased, the output voltage drop during

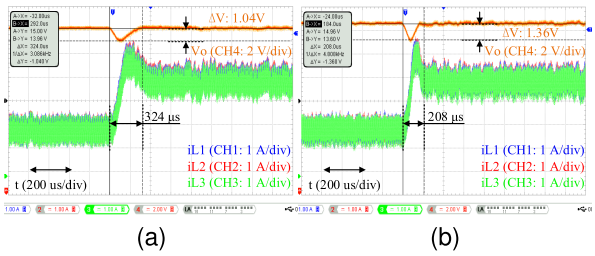

Fig. 21. Experimental test of load disturbance when capacitance parameters are varied. (a) Output capacitance is increased to 200 μF. (b) Output capacitance is reduced to 100 μF.

loading is 1.16 V with the dynamic recovery time of 252 μs. Conversely, $-$15% deviations yield identical voltage deviation magnitudes, but prolonged transient durations extending to 272 μs.

There is no significant change in the system performance during transient process, but the steady state performance is deteriorated by the increase in inductance parameter. Therefore, reducing the controller inductance design parameters within a certain range will not significantly deteriorate the dynamic performance of the system, but can improve its steady-state characteristics, which is basically consistent with the simulation results. To simulate the mismatch of capacitor parameters, the output capacitance is increased and decreased by 50 μF, respectively, the output capacitance is adjusted to 100 and 200 μF, respectively, through the external capacitor board, and the experimental results of load step are shown in Fig. 21. When the output capacitance is 100 μ F, the output voltage drop during loading is 1.36 V, and the dynamic recovery time is 208 μs. The output voltage variation increases by 0.2 V, the regulation time is shortened accordingly, and the voltage and current ripples increase significantly. When the output capacitance is 200 μF, the output voltage drop during loading is 1.04 V, the regulation time becomes longer to 324 μs, and the steady state performance of the output voltage is also improved. This indicates that the capacitor parameters have a large impact on the system performance, and special attention needs to be paid to the capacitor design when using the MFPC. At the same time, the controller parameters should be designed so that the capacitance parameter is smaller than the actual output capacitance to improve the steady state performance.

To test the observer bandwidth and the reference following performance of the converter, a sinusoidal ac signal with amplitude of 1 V and frequency of 3 kHz is superimposed on a 15 V fixed reference, and the experimental results are shown in Fig. 22. The peak-to-peak value of the ac component of the output voltage at 50% rated load is 1.44 V, which is 72% of the ac component of the reference, and the output voltage has good sinusoidal degree and no frequency distortion, so the system has good reference following performance. The output ac component is 1.40 V at rated load, and the bandwidth of the system does not change much. In order to minimize the effect of sampling noise, the observer bandwidth and the controller gain are reduced. As a result, the actual system bandwidth is smaller than the simulation result.

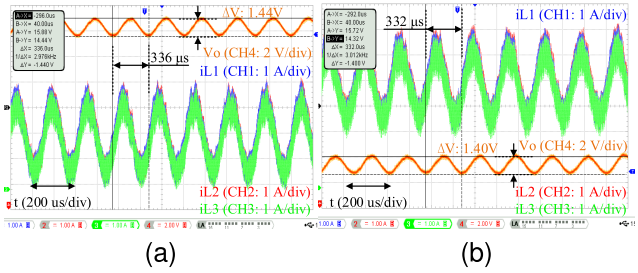

Fig. 22. Experimental test of sinusoidal reference input. (a) Load current is 6 A. (b) Load current is 12 A.

VI. Conclusion

This article introduces a HESO-based MFPC strategy to confront the challenges posed by uncertain or highly time-varying model parameters in certain application scenarios. To reduce the computational complexity associated with algebraic parameter identification, LESO is first introduced for inductor current control, along with a detailed design method for both the LESO and controller gain. Furthermore, the proposed approach effectively mitigates the output voltage overshoot caused by cumulative error in disturbance terms due to parameter deviations in the voltage outer-loop model. In contrast to the PI regulator, it does not require accurate model parameters and has strong robustness. Compared with the LESO-MPFC mehtod, the proposed control algorithm has better transient performance and anti-interference capability. Moreover, when the inductor–capacitor parameters are varied within a certain range, the transient response of the system is maintained. Although the effectiveness of the proposed method is demonstrated on a buck converter, it can be extended to the nonresonant dc–dc converter with a double-closed-loop control structure.

References

[1] A. Villarruel-Parra and A. J. Forsyth, "Modeling phase interactions in the dual-interleaved buck converter using sampler decomposition," *IEEE Trans. Ind. Electron.*, vol. 66, no. 5, pp. 3316–3322, May 2019.

[2] V. Repecho, D. Biel, R. Ramos-Lara, and P. G. Vega, "Fixed-switching frequency interleaved sliding mode eight-phase synchronous buck converter," *IEEE Trans. Power Electron.*, vol. 33, no. 1, pp. 676–688, Jan. 2018.

[3] C. Zhang, Y. Shang, Z. Li, and N. Cui, "An interleaved equalization architecture with self-learning fuzzy logic control for series-connected battery strings," *IEEE Trans. Veh. Technol.*, vol. 66, no. 12, pp. 10923–10934, Dec. 2017.

[4] Q. Xu, N. Vafamand, L. Chen, T. Dragičević, L. Xie, and F. Blaabjerg, "Review on advanced control technologies for bidirectional DC/DC converters in DC microgrids," *IEEE Trans. Emerg. Sel. Topics Power Electron.*, vol. 9, no. 2, pp. 1205–1221, Apr. 2021.

[5] Y. Xie, R. Ghaemi, J. Sun, and J. S. Freudenberg, "Model predictive control for a full bridge DC/DC converter," *IEEE Trans. Control Syst. Technol.*, vol. 20, no. 1, pp. 164–172, Jan. 2012.

[6] X. Liu, D. Wang, and Z. Peng, "A computationally efficient FCS-MPC method without weighting factors for NNPCS with optimal duty cycle control," *IEEE/ASME Trans. Mechatron.*, vol. 23, no. 5, pp. 2503–2514, Oct. 2018.

[7] V. K. Singh, R. N. Tripathi, and T. Hanamoto, "Implementation strategy for resource optimization of FPGA-based adaptive finite control set-MPC using XSG for a VSI system," *IEEE Trans. Emerg. Sel. Topics Power Electron.*, vol. 9, no. 2, pp. 2066–2078, Apr. 2021.

[8] B. Talbi, F. Krim, A. Laib, A. Sahli, and A. Krama, "Pi-mpc switching control for dc-dc boost converter using an adaptive sliding mode observer," in *Proc. 2020 Int. Conf. Elect. Eng.*, 2020, pp. 1–5.

[9] C. Løvaas, M. M. Seron, and G. C. Goodwin, "Robust output-feedback mpc with integral action," *IEEE Trans. Autom. Control*, vol. 55, no. 7, pp. 1531–1543, 2010.

[10] M. E. Albira and M. A. Zohdy, "Adaptive model predictive control for dc-dc power converters with parameters' uncertainties," *IEEE Access*, vol. 9, pp. 135121–135131, 2021.

[11] X. Liu, L. Qiu, Y. Fang, K. Wang, Y. Li, and J. Rodríguez, "A fuzzy approximation for FCS-MPC in power converters," *IEEE Trans. Power Electron.*, vol. 37, no. 8, pp. 9153–9163, Aug. 2022.

[12] B. Zhu, Z. Zheng, and X. Xia, "Constrained adaptive model-predictive control for a class of discrete-time linear systems with parametric uncertainties," *IEEE Trans. Autom. Control*, vol. 65, no. 5, pp. 2223–2229, May 2020.

[13] A. Dhar and S. Bhasin, "Indirect adaptive MPC for discrete-time LTI systems with parametric uncertainties," *IEEE Trans. Autom. Control*, vol. 66, no. 11, pp. 5498–5505, Nov. 2021.

[14] A. Brosch, S. Hanke, O. Wallscheid, and J. Böcker, "Data-driven recursive least squares estimation for model predictive current control of permanent magnet synchronous motors," *IEEE Trans. Power Electron.*, vol. 36, no. 2, pp. 2179–2190, Feb. 2021.

[15] L. Wang, Y. Wang, C. Liu, D. Yang, and Z. Chen, "A power distribution strategy for hybrid energy storage system using adaptive model predictive control," *IEEE Trans. Power Electron.*, vol. 35, no. 6, pp. 5897–5906, Jun. 2020.

[16] X. Li and R. Kennel, "General formulation of kalman-filter-based online parameter identification methods for VSI-Fed PMSM," *IEEE Trans. Ind. Electron.*, vol. 68, no. 4, pp. 2856–2864, Apr. 2021.

[17] O. Babayomi, Z. Zhang, Y. Li, and R. Kennel, "Adaptive predictive control with neuro-fuzzy parameter estimation for microgrid grid-forming converters," *Sustainability*, vol. 13, no. 13, pp. 1–17, 2021.

[18] S. Gao, H. Dong, B. Ning, T. Tang, and Y. Li, "Nonlinear mapping-based feedback technique of dynamic surface control for the chaotic pmsm using neural approximation and parameter identification," *IET Control Theory Appl.*, vol. 12, no. 6, pp. 819–827(8), Apr. 2018.

[19] X. An, G. Liu, Q. Chen, W. Zhao, and X. Song, "Adjustable model predictive control for IPMSM drives based on online stator inductance identification," *IEEE Trans. Ind. Electron.*, vol. 69, no. 4, pp. 3368–3381, Apr. 2022.

[20] M. A. Hamida, J. De Leon, A. Glumineau, and R. Boisliveau, "An adaptive interconnected observer for sensorless control of PM synchronous motors with online parameter identification," *IEEE Trans. Ind. Electron.*, vol. 60, no. 2, pp. 739–748, Feb. 2013.

[21] M. Martinez, D. Reigosa, D. Fernández, J. M. Guerrero, and F. Briz, "Enhancement of permanent-magnet synchronous machines torque estimation using pulsating high-frequency current injection," *IEEE Trans. Ind. Appl.*, vol. 56, no. 1, pp. 358–366, Jan.-Feb. 2020.

[22] Z. Li, G. Feng, C. Lai, D. Banerjee, W. Li, and N. C. Kar, "Current injection-based multi-parameter estimation for dual three-phase IPMSM considering VSI nonlinearity," *IEEE Trans. Transport. Electrific.*, vol. 5, no. 2, pp. 405–415, Jun. 2019.

[23] J. Yang, W. X. Zheng, S. Li, B. Wu, and M. Cheng, "Design of a prediction-accuracy-enhanced continuous-time MPC for disturbed systems via a disturbance observer," *IEEE Trans. Ind. Electron.*, vol. 62, no. 9, pp. 5807–5816, Sep. 2015.

[24] X. Zhang, B. Hou, and Y. Mei, "Deadbeat predictive current control of permanent-magnet synchronous motors with stator current and disturbance observer," *IEEE Trans. Power Electron.*, vol. 32, no. 5, pp. 3818–3834, May 2017.

[25] J. Rodrıguez, R. Heydari, Z. Rafiee, H. A. Young, F. Flores-Bahamonde, and M. Shahparasti, "Model-free predictive current control of a voltage source inverter," *IEEE Access*, vol. 8, pp. 211104–211114, 2020.

[26] M. Khalilzadeh, S. Vaez-Zadeh, J. Rodriguez, and R. Heydari, "Model-free predictive control of motor drives and power converters: A review," *IEEE Access*, vol. 9, pp. 105733–105747, 2021.

[27] K.-J. Lee, B.-G. Park, R.-Y. Kim, and D.-S. Hyun, "Robust predictive current controller based on a disturbance estimator in a three-phase grid-connected inverter," *IEEE Trans. Power Electron.*, vol. 27, no. 1, pp. 276–283, Jan. 2012.

[28] M. Siami, D. A. Khaburi, A. Abbaszadeh, and J. Rodrıguez, "Robustness improvement of predictive current control using prediction error correction for permanent-magnet synchronous machines," *IEEE Trans. Ind. Electron.*, vol. 63, no. 6, pp. 3458–3466, Jun. 2016.

[29] H. Li, J. Shao, and Z. Liu, "Incremental model predictive current control for PMSM with online compensation for parameter mismatch," *IEEE Trans. Energy Convers.*, vol. 38, no. 2, pp. 1050–1059, Jun. 2023.

[30] C.-K. Lin, T.-H. Liu, J.-t. Yu, L.-C. Fu, and C.-F. Hsiao, "Model-free predictive current control for interior permanent-magnet synchronous motor drives based on current difference detection technique," *IEEE Trans. Ind. Electron.*, vol. 61, no. 2, pp. 667–681, Feb. 2014.
[31] C. Ma, H. Li, X. Yao, Z. Zhang, and F. De Belie, "An improved model-free predictive current control with advanced current gradient updating mechanism," *IEEE Trans. Ind. Electron.*, vol. 68, no. 12, pp. 11968–11979, Dec. 2021.
[32] M. Fliess and C. Join, "Model-free control," *Int. J. Control*, vol. 86, no. 12, pp. 2228–2252, 2013.
[33] Y. Zhou, H. Li, R. Liu, and J. Mao, "Continuous voltage vector model-free predictive current control of surface mounted permanent magnet synchronous motor," *IEEE Trans. Energy Convers.*, vol. 34, no. 2, pp. 899–908, Jun. 2019.
[34] Y. Zhang, J. Jin, and L. Huang, "Model-free predictive current control of PMSM drives based on extended state observer using ultralocal model," *IEEE Trans. Ind. Electron.*, vol. 68, no. 2, pp. 993–1003, Feb. 2021.

Yang Liu (Senior Member, IEEE) received the M.E. and Ph.D. degrees in control science and engineering from the Department of Control Science and Engineering, School of Automation, Huazhong University of Science and Technology (HUST), Wuhan, China, in 2005 and 2009, respectively.

He is currently an Associate Professor with the School of Artificial Intelligence and Automation, HUST. His research interests include power electronics using SiC and GaN, high performance ac motor drives, and fault diagnosis of power converters.

Xiaoya Mi was born in Shaanxi Province, China, in 1998. She received the B.Eng. degree in control science and engineering from Huazhong University of Science and Technology (HUST), Wuhan, China, in 2024. She is currently working toward the M.S. degree in control science and engineering with the School of Artificial Intelligence and Automation. Her research interests include MPC and advanced control strategies for power electronics and converters.

Peng Zhang was born in Shaanxi Province, China, in 1998. He received the B.S. degree in control science and engineering from the Department of Control Science and Engineering, School of Automation, Huazhong University of Science and Technology, Wuhan, China, in 2021, and the M.S. degree in control science and engineering from the School of Artificial Intelligence and Automation, Huazhong University of Science and Technology, in 2024.

His research interests include model predictive control and dc–dc converter.

Yongheng Yang (Senior Member, IEEE) received the B.Eng. degree in electrical engineering and automation from Northwestern Polytechnical University, Xi'an, China, in 2009, and the Ph.D. degree in energy technology from Aalborg University, Denmark, in 2014. From 2009 to 2011, he received the Postgraduate Studies with Southeast University, Nanjing, China.

From 2013, he was a Visiting Scholar with Texas A&M University, College Station, TX, USA. From 2014 to 2020, he was associated with the Department of Energy Technology, Aalborg University, Aalborg, Denmark, where he achieved the rank of tenured Associate Professor in 2018. In January 2021, he joined Zhejiang University, Hangzhou, China, as a ZJU100 Professor. His research interests include grid-friendly integration of photovoltaic systems and control of power converters, specifically grid-forming technologies.

Dr. Yang was the recipient of the 2018 IET Renewable Power Generation Premium Award and was recognized as an Outstanding Reviewer for the IEEE TPEL in 2018, the 2021 Richard M. Bass Outstanding Young Power Electronics Engineer Award from the IEEE Power Electronics Society (PELS) and the 2022 IEEJ Isao Takahashi Power Electronics Award. He became a Zhejiang Topnotch Scholar in 2023, awarded to him to tackle the issues for large-scale grid integration of renewable energy. In addition, he has received three IEEE Best Paper Awards, and the Excellent Paper Award of CSEE Journal of Power and Energy Systems in 2023. He has been included on the Highly Cited Chinese Researchers list by Elsevier since 2021. He is presently a Council Member of the China Power Supply Society. He curently serves as an Associate Editor for IEEE TRANSACTIONS ON POWER ELECTRONICS (IEEE TPEL)and IEEE TRANSACTIONS ON SUSTAINABLE ENERGY.

Chunyang Zheng received the M.Eng. degree in control science and engineering from the Harbin Institute of Technology, Harbin, China, in 2011. He is currently working toward the Ph.D. degree in control science and engineering with the School of Artificial intelligence and Automation, Huazhong University of Science and Technology, Wuhan, China.

From 2018 to present, he has served as the General Manager of Intelligent Control System Company Ltd. Under his leadership, the company has focused on the electric control business and delivered leading electric control solutions. From 2011 to 2017, he was employed with Shenzhen Hangsheng Electronics, where he held positions including Senior Electric Control Software Engineer, Product Manager, Director, and CTO. During this time, he spearheaded the platform planning and technical development for the company's three major product lines: MCU, BMS and VCU. His research interests include power electronics using IGBT and SiC, architecture and algorithm of power domain control in application of new energy vehicles.

Mr. Zheng was the recipient of "China Patent Excellence Award" as the first inventor in 2018. In 2020, he was awarded the title of "Shenzhen Municipal-level Leading Talent". He was honored as one of "Shenzhen's First Batch of Young Innovative and Entrepreneurial Talents" in 2016. '.

Yuxuan Pei was born in Hunan Province, China, in 1996. He received the M.S. degree in mechanical engineering from College of Mechanical and Vehicle Engineering, Hunan University, Changsha, China, in 2022.

He is currently an Engineer with Beijing Trinova Technology Company Ltd. His research interests include high performance ac motor drives and vehicle dynamic control.